Appl. Phys. A (2017) 123:727
DOI 10.1007/s00339-017-1346-y

Applied Physics A
Materials Science & Processing

# Stabilized gold nanoparticles by laser ablation in ferric chloride solutions

**M. I. Nouraddini[1] · M. Ranjbar[1] · P. J. Dobson[2] · H. Farrokhpour[3] · C. Johnston[4] · K. Jurkschat[4]**

Received: 3 July 2017 / Accepted: 27 October 2017


**Abstract** In this study, laser ablation of gold was performed in different ferric chloride solutions and water as a reference. The ferric chloride solutions included hexachloro iron(III) and aquachloro iron(III) having low and high hydrolysis degree. Transmission electron microscope (TEM) images showed spherical gold nanoparticles (GNPs) in water, particles which are strongly agglomerated with intimate contact at their interfaces in hexachloro iron(III) and individual separated particles with a halo of an iron component in aquachloro iron(III). In addition, no combination of Au and Fe was found in HAADF analysis or X-ray diffraction (XRD) patterns. In optical investigations, it was observed that gold nanoparticles made in hexachloro iron(III) solutions have localized surface plasmon resonance (LSPR) peaks broader than in the case of water that are quenched after a few hours, while ablation in the aquachloro iron(III) solution provides narrow LSPR absorption with a long-term stability. According to X-ray photoelectron spectroscopy (XPS) there are metallic Au and $Fe^{2+}$ states in the drop-casted samples. By comparison of cyclic voltammetry of solutions before and after laser ablation, strong agglomeration in hexachloro iron(III) was attributed to the reducing role of iron(III) creating an unstable gold surface in the chloride solution. In aquachloro iron(III), however, the observed stability was attributed to the formation of the halo of an iron compound around the particles.

✉ M. Ranjbar
ranjbar@cc.iut.ac.ir

[1] Department of Physics, Isfahan University of Technology, Isfahan 8415683111, Iran

[2] The Queen's College, Oxford OX1 4AW, UK

[3] Department of Chemistry, Isfahan University of Technology, Isfahan 8415683111, Iran

[4] Department of Materials, Oxford University, Begbroke Science Park, Sandy Lane, Yarnton, Oxford OX5 1PF, UK

## 1 Introduction

In recent years, colloidal noble-metal NPs have had spectacular development because of their peculiar physical and chemical properties such as interesting optical, catalytic, electronic and magnetic properties which are particularly different and unique in comparison to bulk samples [1–6]. Numerous properties that impact on the new effects include the appearance of electronic and atom-packing shell structures, along with altered interactions among the nanoparticles [7]. These effects relate to quantum confinement effects in the nanoscale with respect to bulk [8] and to enhanced surface activity due to a large surface to volume ratio [9]. Gold and silver NPs are probably the most attractive noble metal nanostructures because of their unique and interesting physical and chemical properties [1, 10–12]. GNPs have application in surface-enhanced Raman scattering (SERS) [13, 14], LSPR [1, 14–21], non-linear optical properties (NLO) [22] and quantized charging effects [23].

However, the long-term stability of GNPs suffers from quenching due to surface passivation and agglomeration that aging applies to all of them. Up to now, many attempts have been made for long-term stabilization of GNPs using a number of chemical ligands [24–26]. Various compounds such as, cyclodextrin, surfactants and thiol compounds have been used to improve the stability of GNPs [27]. A stabilizer should have minimum toxicity, a suitable atomic link to combine with gold and some additional functionality.

The combination of the magnetic and optical elements in one single entity promises multifunctionality, so there has been considerable interest to combine Au nanoparticles and

Published online: 02 November 2017

a magnetic element such as iron to provide magnetic–plasmonic effects [28–32] for diagnosis [33, 34] and photocatalytic applications [35]. Although various methods [34, 36–42] have been used so far for synthesis of Au–Fe NPs, the combination of iron and gold does not readily happen at ordinary pressures and temperatures due to thermodynamic considerations [42]. Indeed, the Fe-Au system has a positive heat of mixing, phase separation is energetically favored and as a consequence solubility of Fe in Au is restricted to less than 2% at room temperature [43]. This difficulty of combining iron and gold can be used as a method to produce GNPs with acceptable purity and stability.

The method of laser ablation synthesis in liquid (LASiS) is a new way of carrying out the synthesis of noble-metal NPs and is an efficient approach for preparing various nanoscale materials [44–47]. In this method, by irradiating a target by a pulsed laser beam, the target elements, in the form of vapourized atoms in a bubble form are directly removed from the surface [48]. These atoms condense to form nanoparticles as they propagate throughout the liquid and they react with the liquid medium [49, 50]. The LASiS technique gives products with high purity due to direct interaction of laser beam, and allows for synthesis in short times at ambient temperature with a vast compositional range of both target and solvent with possible stability [51–53]. There are two different approaches for fabrication of multi-particles by LASiS: the laser ablation of alloy targets in nonreactive solutions like DI water and alcohols, or laser ablation of a metallic target in a reactive solution. Recently, LASiS has been successfully applied to fabricate Au–Fe metastable nanoparticles using Au–Fe alloy targets [42] where the effect of the chemical environment on the structure and composition of metastable nanoalloys was explored but the stability of GNPs has remained unclear. To the best of our knowledge, no report exists on the laser ablation of gold in an iron solution such as ferric chloride. We have previously reported laser ablation of gold in palladium chloride solution and observed formation of core–shell structures of Au/Pd(II) via a reduction reaction process [54]. There was observed instability for GNPS due to replacement reaction of gold and palladium. Due to the low reactivity of gold and iron, laser ablation of gold in a ferric ion solution may create stabilized GNPs. Despite the difficulty of combining iron and gold, iron ions can reduce the gold ions to gold metal and enhance agglomeration. However, dissolving iron(III) chloride in water is an exothermic process and leads to hydrolysis. If the solution is acidified in different ways, different degrees of hydrolysis are obtained. Our study revealed that the degree of hydrolysis of ferric chloride solution has a great impact on gold nanoparticles' stability produced by the LASiS method. Therefore, the main contribution of this study is to produce GNPs by laser ablation of gold in ferric chloride solution and show the role of solutions on the product stability. GNPs in DI water were also prepared as a reference sample for comparison. Our investigations by XRD, UV–Vis and HRTEM revealed that GNPs shape, LSPR peaks and the most likely important issue, stability, depends on the media used for the ablation.

## 2 Experimental

For laser ablation of gold, a beam of a Nd:YAG laser ($\lambda = 1064$ nm, $\tau = 5$ ns, R.R = 10 Hz, 360 mJ energy per pulse and 30 min laser ablation) is directed into the solution by means of a mirror and a lens and is perpendicularly focused on the surface of a gold target (purity of 99.99%) placed inside the glass vessel. The spot size of the focused beam at the target surface was 1 $mm^2$. Three different samples of ablation were prepared and named accordingly. Sample S1 was prepared by laser ablation of gold target in 100 ml DI water as a reference. Sample S2 was prepared in an hexachloro iron(III) colorless ferric chloride solution providing an environment with a low degree of hydrolysis (Table 1). To prepare this solution HCl (37%) (0.1 ml) + DI water (100 ml) was stirred by an ultrasound bath, then $FeCl_3.6H_2O$ (Merck 98%) (0.03 gr) was dissolved and the resultant solution was stirred again. For sample S3, a brown aquachloro iron(III) ferric chloride solution was prepared by dissolving $FeCl_3.6H_2O$ (0.03 gr) in 100 ml DI water followed by sonication, then 0.1 ml HCl was added and the resultant was stirred again. In this way, the solution has a high degree of hydrolysis. Therefore, the only difference in producing hexachloro iron and hydrochloro iron is the reversed order of HCl and $FeCl_3$ addition. The pH of both solutions was about 2.2. Then the effect of aging was studied by UV–Vis spectrometry. Figure 1 shows the schematic representation of laser ablation of gold in different solutions and the effect of aging. Using inductively coupled plasma optical emission spectroscopy (ICP-OES) (Optima 7300 DV) analysis concentrations of gold and iron were determined (Table 1). The shape and morphology of the NPs were observed by high resolution transmission electron microscopy (HRTEM) and high angle annular dark field (HAADF) scanning transmission electron microscopy (STEM) (JEOL 2010 FX 200 keV and JEOL

**Table 1** Au and Au–Fe sample preparation conditions by laser ablation method

| Sample code | Solution | ICP concentration (ppm) | |
|---|---|---|---|
| | | Au | Fe |
| S1 | DI water | 19.8 | – |
| S2 | Hexachloro iron(III) | 12.5 | 88.7 |
| S3 | Aquachloro iron(III) | 35.6 | 86.5 |

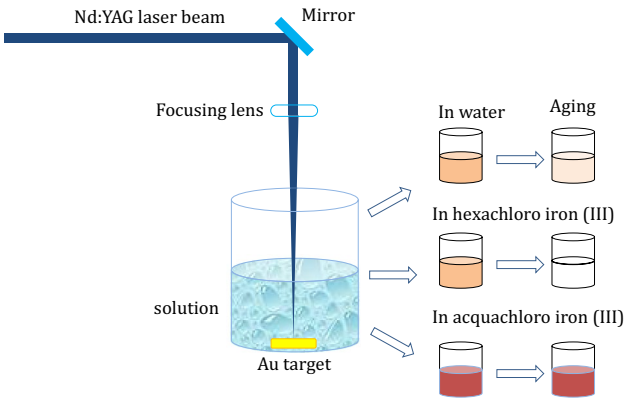


**Fig. 1** Schematic representation of laser ablation of golf in water and ferric chloride solutions and the effect of aging

3000F 300 keV). The crystalline structure of the samples was characterized using an X-ray diffractometer (Philips EXPERTMPD) with Cu-Kα ($\lambda = 0.154$ nm) radiation. XPS was done in an ESCA/AES system equipped with a concentric hemispherical analyzer (CHA, Specs model EA10 plus). Optical properties of the solutions of the samples were measured in the 200–1100 nm wavelength range using a Lambda 25 spectrophotometer (Perkin Elmer). Cyclic voltammetry (CV) experiments were performed using a classical three-electrode configuration (Iviumstat electrochemical analyzer, Ivium Technology). The CV curves were measured at 200 mV/s scan rate and Ag/AgCl as reference electrode.

## 3 Results and discussion

Figure 2a–c top panel shows the TEM images of the nanoparticles in samples S1, S2 and S3, respectively. The TEM images of sample S1 reveals a chain of spherical GNPs. Formation of nanoparticle chains is due to the linear aggregation because of the dipole–dipole interaction in the solution [55]. The lattice spacing of these spherical particles shown in the bottom panel is consistent with (111) plane of metallic gold. The image of sample S2 shows nanoparticles in an aggregated 2 or 3D network. The network configurations consist of nanoparticles that are strongly attached to each other. HRTEM and IFFT images from different points of a conjugated particle and its interface are shown in the lower panel. The IFFT of the conjugated particles interface indicates clearly that two parts of the particles are attached to each other via a crystalline interface. Therefore, an intimate

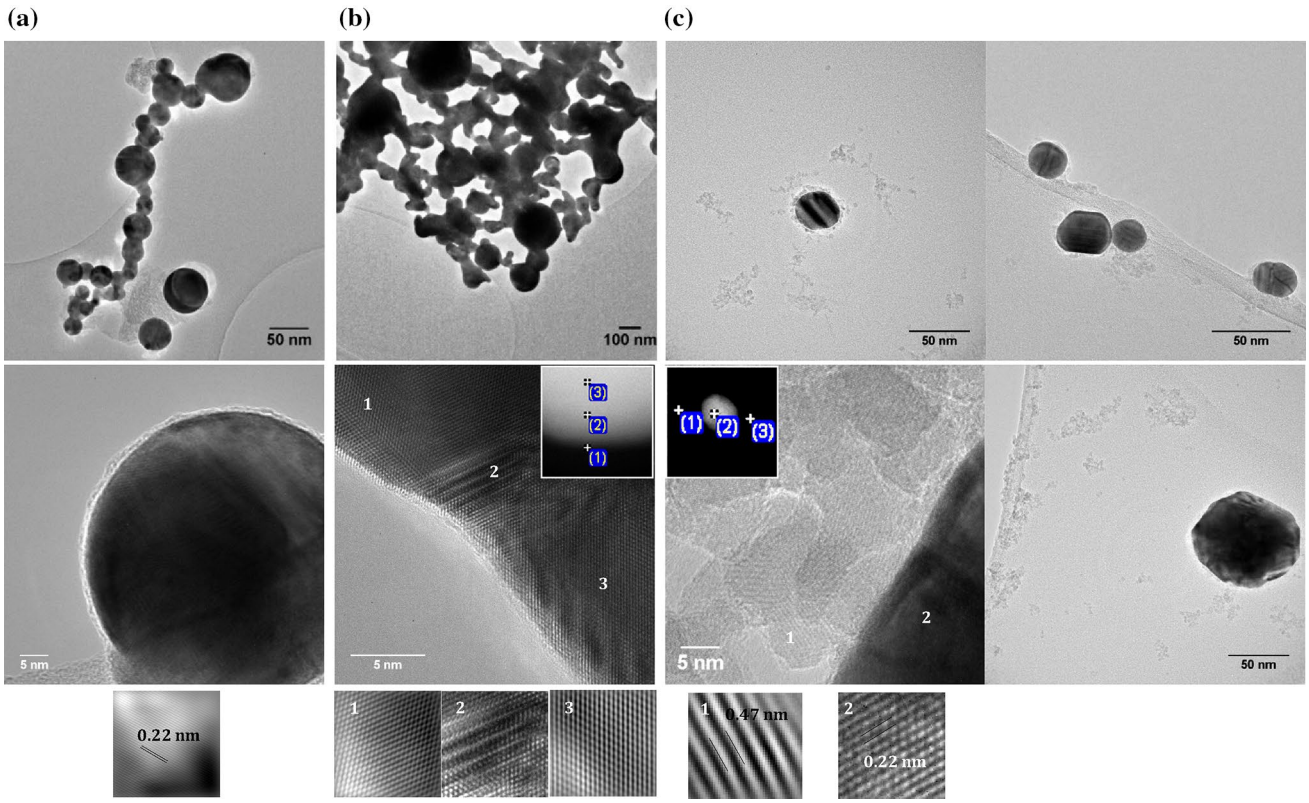


**Fig. 2** TEM, HRTEM and IFFT images from selected zones of sample **a** S1 **b** S2, and **c** S3 recorded after laser ablation. Inset of part **b** and **c** indicates the HDAAF images of single particles. In HDAAF of part **b** points 2 and 3 are gold which is free of iron, in part **c** points 1 and 3 are iron-rich without gold and point 2 is gold-rich without iron

contact exists between two gold nanoparticles at the interfaces. The coagulation of nanoparticles observable in the image indicates a strong tendency for strong agglomeration of gold in the presence of hexachloro iron(III). A selected HAADF image in the inset of Fig. 2b revealed that (points 2 and 3) there is no iron in the nanoparticle region and its surrounding (point 1). In the TEM image of sample S3, however, a single Au nanoparticle with a gray contrast halo around it can be clearly seen. No agglomeration or chain formation was observed for S3 and almost all TEM images included single or a few number of particles. Similar single GNPs without agglomeration are shown in Fig. 2c. In addition to this halo, a number of agglomerated smaller particles with the same gray contrast are observable around it. The HRTEM and IFFT images from the gray and dark regions are shown in the bottom panel. The gray contrast particles have a lattice spacing of about 0.47 nm while the dark particles are believed to be gold with about 0.22 nm lattice spacing. The HAADF image confirms that the particles are gold and the halo in its vicinity comprises entirely of iron. Therefore, the gray contrast particles are attributed to an iron compound that acts as protecting layer against agglomeration around the particle.

To investigate the structure of the GNPs, XRD was used. The XRD patterns from sample S1, S2 and S3 after centrifuging and drop-casting on amorphous glass substrates are shown in Fig. 3. The patterns of all the samples represent (111), (200), (220) and (311) peaks which are assigned to the fcc cubic crystal structure of gold (JCPDS card number 00-001-1174). All the diffraction peaks of the metallic Fe (JCPDS card number 01-085-1410), however, overlap

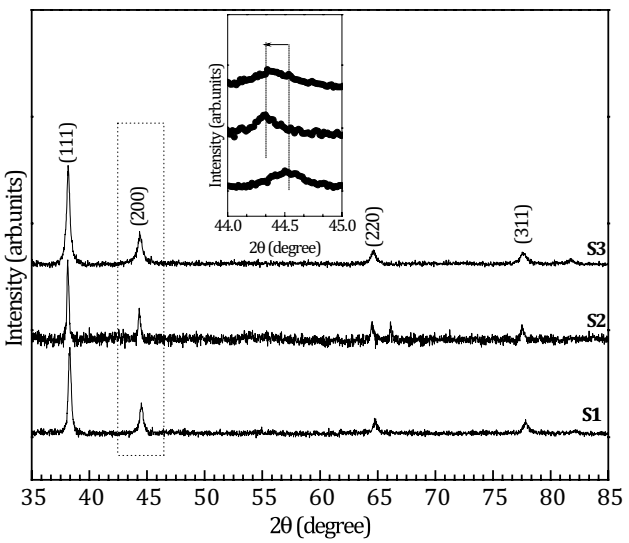


**Fig. 3** XRD patterns of drop-casted samples of S1, S2 and S3. Inset shows the high magnification detail at $2\theta \sim 44.5^{\circ}$

those of fcc gold metal. Therefore, it is not so straightforward to determine whether or not peaks corresponding to iron exist in the patterns of samples S2 and S3. However, comparing the XRD patterns of S2 and S3 with that of S3 indicates they have similar relative intensities and no trace of metallic iron should be found. In addition, no diffraction peak or trace of oxide or chloride phases for gold and iron were seen. The only difference is that the high magnification window around $2\theta \sim 44.5^{\circ}$ (inset) indicates that sample S3 has relatively broader peaks. Moreover, the peaks in samples S2 and S3 undergo a shift toward lower $2\theta$ values indicating an increase in the lattice parameter of gold from $a = 4.064$–$4.078$ Å. According to XRD it can be inferred that the ablation of gold in iron chloride has no considerable impact on the purity of gold nanoparticles.

XPS was also used to study the chemical composition of nanoparticles. Before XPS, the samples were sonicated, centrifuged and drop-casted on glass substrates. High resolution XPS spectra and peak fitting of a typical $Au_{4f}$ region and $Fe_{2p}$ regions of iron are shown in Fig. 4a–c. The spin–orbit splitting of $Au_{4f7/2}$ and $Au_{4f5/2}$ is about 3.6 eV. The $Au_{4f7/2}$ and $Au_{4f5/2}$ peaks have binding energy at about 84 and 87.5 eV, respectively which is characteristic of $Au^0$. The position of $Fe_{2p3/2}$ at 712.2 and $Fe_{2p1/2}$ at 725.5 eV corresponds to the $Fe^{2+}$ oxidation state in both samples S2 and S3. The existence of the $Fe^{2+}$ oxidation state can be also attributed to slightly surface oxidation of Fe in the drying process.

The aging investigation is performed to compare the effect of the ablation medium on the stability of LSPR absorption peaks of colloidal GNPs over time. Successive UV–Vis absorption spectra of samples taken in different steps within an aging period from 10 min to 2 days after laser ablation are shown in Fig. 5. The photographic images of colloidal samples taken at different aging times including before, just after and 2 days after laser ablation are also presented. Hexachloro iron(III) solution is colorless and the aquachloro iron(III) solution light brown before laser ablation. Laser ablation of gold target in water and in hexachloro iron(III) lead to purple solutions (sample S1 and S2). However, in preparation of the sample S3, a dark red color appears upon laser ablation. All the samples S1, S2 and S3 have different LSPR peaks early after ablation but all center around the 550 nm characteristic of the plasmonic feature for gold nanoparticles in an aqueous medium [19]. A significant difference, however, exists between their LSPR shape and aging stability. The time variations of LSPR maxima are also presented. The absorption intensity decreases exponentially with a slight slope for S1 and with a steeper slope to zero for S2, whilst it almost increases initially for S3 before falling slightly. For sample S1, about 115 min following the laser ablation, the LSPR peak damps and the maximum absorption of the LSPR reduces from about 0.25 to about

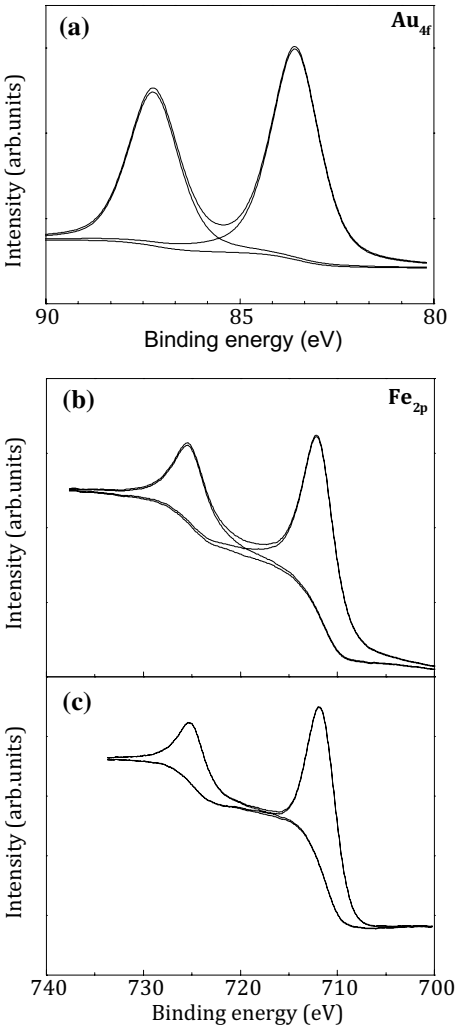


**Fig. 4** **a**–**c** High resolution XPS spectra of typical Au4f and Fe2p

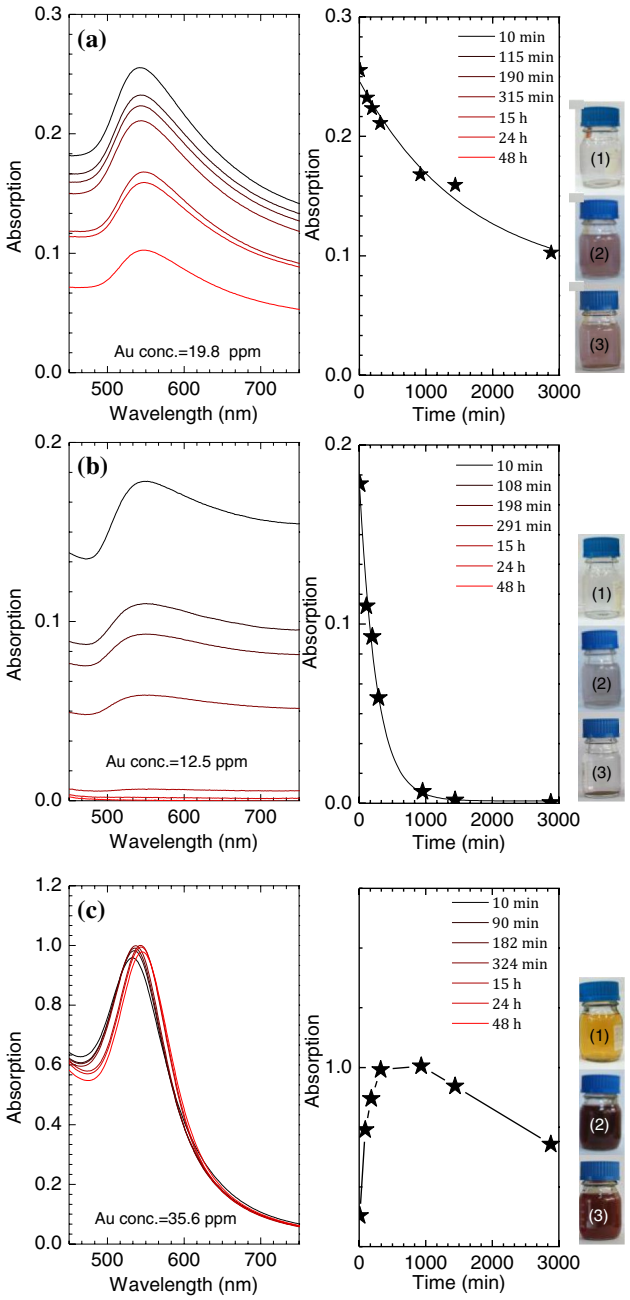


**Fig. 5** Successive optical absorption spectra of samples **a** S1, **b** S2 and **c** S3. Middle panels indicate the corresponding time variation of peak values and ICP concentrations of gold. Photographic images at different stage of process are shown in the right panels: (1) before, (2) just after and (3) 2 days after laser ablation of gold

0.1 during 2 days (~3000 min) of aging. Sample S2 shows a LSPR peak smaller and considerably broader in comparison to sample S1 and S3 which damps quickly with age. Precipitation was also observed for sample S2 for which any attempts by sonication to recover the plasmonic peak failed. This is attributed to sedimentation and agglomeration-induced broadening of the plasmon resonance. However, sample S3 interestingly has a stronger LSPR intensity, about ten times higher than S2, and a narrow LSPR peak in comparison and an excellent aging stability without any precipitation of nanoparticles. The increase of the LSPR intensity in sample S3 early after the LASiS process is likely to result from the post-formation of new Au particles or growth of existing seed particles previously formed in the suspension. So the Au LSPR peak clearly depends on the ablation medium and there is a significant difference between the two types of ferric chloride solutions used as the ablation environment. The different amount of ablated Au (Au conc.) in the samples shows the effective role of the ablation environment. Sample S3 with the highest Au colloidal NPs concentration has the highest maximum absorption intensity, while S2 has the lowest one. It is consistent with the Beer–Lambert law, implying a proportional relation between LSPR absorption intensity and the concentration of

colloidal NPs. Optical spectroscopy data indicates clearly that laser ablation in aquachloro iron(III) leads to a very stable gold solution and based on XRD and HAADF without any combination with iron.

The concentration of iron ions in the laser ablation process may be responsible for the different stability observed for samples. Cyclic voltammetry of the solution before and after the laser ablation can be useful to get information on the variation of ionic species. Figure 6 shows the CV curves (scan rate 200 mV/s) for two types of ferric chloride solutions before and after laser ablation of gold. Hexachloro iron(III) and aquachloro iron(III) exhibit different electrochemical behaviors before gold ablation. As can be seen, both oxidation and reduction peaks of hexachloro iron(III) is much higher than in aquachloro iron(III). Since the measured CV current is in direct proportion to the iron ion concentration, hexachloro iron(III) contains much higher ionic species of iron. After laser ablation, a decrease in CV current of S2 and an increase in sample S3 is clearly observable. This shows that laser ablation in hexachloro iron(III) is accompanied by consumption of iron ions while in sample S3 no reducing action was observed and new iron ions are generated spontaneously due to aging.

If the behavior of sample S1 is attributed to normal agglomeration and precipitation of GNPs in DI water, we can expect for S2 a greater surface charge neutralization of gold nanoparticles by a chemical/electrostatic interaction between the gold nanoparticle via iron ions and this is a possible reason for steep decrease of LSPR peak. In sample S2, the higher content of iron ions changes the charge balance on the surface of gold nanoparticles resulting in agglomeration of nanoparticles. The reaction at the interface of intimate contacts between Au nanoparticles in sample S2 can be ascribed to the role of iron ions in reduction of gold(III) in the following stages [56]:

$$Au^{3+} + 2Fe^{2+} \rightarrow Au^{1+} + 2Fe^{3+} \quad (1)$$

$$Au^{1+} + Fe^{2+} \rightarrow Au^{0} + Fe^{3+}$$

In the presence of hexachloro iron(III), damping of the LSPR absorption peaks of Au is also attributed to particle–particle agglomeration, a surface passivation by iron ions [57, 58], or a polymerization with existing Fe-OH chains of hexachloro iron(III) due to surface coverage on the GNPs. However, in sample S3, TEM and UV–Vis observations suggest that the layer of aquachloro iron around gold nanoparticles acts as protecting layer against agglomeration and stabilizes them. Therefore, the ablation process in the presence of aquachloro iron maintained the integrity of gold nanoparticles. The consolidation of sample S3 is partially attributed to an hydrolysis assisted solidification (HAS) using iron chloride as a setting agent. The consolidation takes place by the internal consumption of water due to much more hydrolysis of $FeCl_3$ in sample S3. Colloidal gold nanoparticles obtained by laser ablation normally agglomerate in water, but our results indicated that they can be stabilized in aquachloro iron (III) solutions. When two stabilized Au NPs approach each other they experience repulsive forces once the outer shells begin to overlap. In the other words, when ablation is performed in aquachloro iron there is an iron complex that strongly binds to GNPs, increasing the negative charge on the surface and electrostatic repulsion between the particles, further stabilizing the colloidal solution. However, for S2, the cyclic voltammetry suggests that agglomeration may be induced by increasing the ionic strength for instance using HCl before dissolving the iron chloride salt.

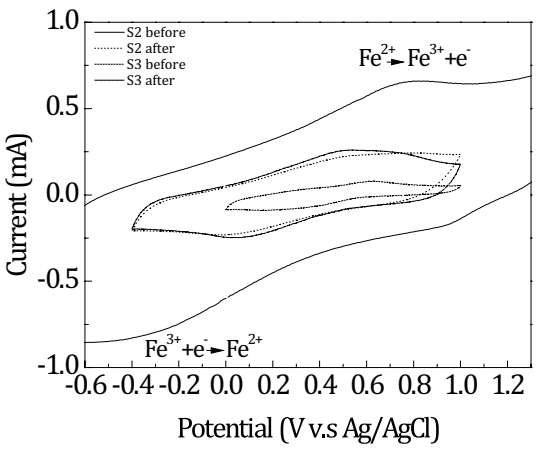


**Fig. 6** Cyclic voltammetry of ferric chloride solutions before and after laser ablation with a scan rate of 200 mV/s

## 4 Conclusion

In summary, laser ablation of gold was performed in water, hexachloro iron(III) and aquachloro iron(III). It was found that compared with the two other media, aquachloro iron(III) leads to very stable nanoparticles with narrow LSPR peaks. The hexachloro iron(III) produced particles with a broad LSPR peak and their stability is even less than in water and the obtained gold nanoparticles are precipitated quickly. Structural analysis by XRD shows that the iron solutions preserve the purity of gold so that iron is not combined with gold. HRTEM showed that the particles in hexachloro iron(III) are often firmly attached together via a crystalline interface and as a result, large agglomerations form. But in aquachloro iron(III) a protective layer consisting of an iron composition keeps particles separated and stable. Gold instability in hexachloro iron(III) is attributed to the presence of

iron ions and its reducing role for reduction of gold at gold nanoparticles interfaces. The stability of nanoparticles in aquachloro iron(III) attributed to high rates of hydrolysis and the role of water in binding with the surface of gold nanoparticles.

## References


1. P.K. Jain et al., Noble metals on the nanoscale: optical and photothermal properties and some applications in imaging, sensing, biology, and medicine. Acc. Chem. Res. **41**(12), 1578–1586 (2008)
2. X. Sun, Y. Li, Colloidal carbon spheres and their core/shell structures with noble-metal nanoparticles. Angew. Chem. Int. Ed. **43**(5), 597–601 (2004)
3. J. Bartolomé et al., Magnetic polarization of noble metals by Co nanoparticles in M-capped granular multilayers (M=Cu, Ag, and Au): an X-ray magnetic circular dichroism study. Phys. Rev. B—Condens. Matter Mater. Phys. **77**(18), 184420 (2008)
4. N. Lopez et al., On the origin of the catalytic activity of gold nanoparticles for low-temperature CO oxidation. J. Catal. **223**(1), 232–235 (2004)
5. C. Gutiérrez-Sánchez et al., Gold nanoparticles as electronic bridges for laccase-based biocathodes. J. Am. Chem. Soc. **134**(41), 17212–17220 (2012)
6. J.P. Sylvestre et al., Femtosecond laser ablation of gold in water: Influence of the laser-produced plasma on the nanoparticle size distribution. Appl. Phys. A: Mater. Sci. Process. **80**(4), 753–758 (2005)
7. H. Qian et al., Total structure determination of thiolate-protected Au38 nanoparticles. J. Am. Chem. Soc. **132**(24), 8280–8281 (2010)
8. M.A. El-Sayed, Some interesting properties of metals confined in time and nanometer space of different shapes. Acc. Chem. Res. **34**(4), 257–264 (2001)
9. M. Wang, D.-j.. Guo, H.-l.. Li, High activity of novel Pd/$TiO_2$ nanotube catalysts for methanol electro-oxidation. J. Solid State Chem. **178**(6), 1996–2000 (2005)
10. S.E. Skrabalak et al., Gold nanocages: synthesis, properties, and applications. Acc. Chem. Res. **41**(12), 1587–1595 (2008)
11. M.C. Daniel, D. Astruc, Gold nanoparticles: assembly, supramolecular chemistry, quantum-size-related properties, and applications toward biology, catalysis, and nanotechnology. Chem. Rev. **104**(1), 293–346 (2004)
12. Y. Sun, Y. Xia, Shape-controlled synthesis of gold and silver nanoparticles. Science **298**(5601), 2176–2179 (2002)
13. Y.C. Cao, R. Jin, C.A. Mirkin, Nanoparticles with Raman spectroscopic fingerprints for DNA and RNA detection. Science **297**(5586), 1536–1540 (2002)
14. P.L. Stiles et al., Surface-enhanced Raman spectroscopy, in Annual Review of Analytical Chemistry. 2008. pp. 601–626
15. J.N. Anker et al., Biosensing with plasmonic nanosensors. Nat. Mater. **7**(6), 442–453 (2008)
16. S. Eustis, M.A. El-Sayed, Why gold nanoparticles are more precious than pretty gold: Noble metal surface plasmon resonance and its enhancement of the radiative and nonradiative properties of nanocrystals of different shapes. Chem. Soc. Rev. **35**(3), 209–217 (2006)
17. X. Huang et al., Cancer cell imaging and photothermal therapy in the near-infrared region by using gold nanorods. J. Am. Chem. Soc. **128**(6), 2115–2120 (2006)
18. E. Hutter, J.H. Fendler, Exploitation of localized surface plasmon resonance. Adv. Mater. **16**(19), 1685–1706 (2004)
19. P.K. Jain et al., Calculated absorption and scattering properties of gold nanoparticles of different size, shape, and composition: Applications in biological imaging and biomedicine. J. Phys. Chem. B **110**(14), 7238–7248 (2006)
20. K.L. Kelly et al., The optical properties of metal nanoparticles: the influence of size, shape, and dielectric environment. J. Phys. Chem. B **107**(3), 668–677 (2003)
21. K.A. Willets, R.P. Van Duyne, Localized surface plasmon resonance spectroscopy and sensing, in *Annual Review of Physical Chemistry*. 2007. pp. 267–297
22. G.K. Darbha et al., Selective detection of mercury (II) ion using nonlinear optical properties of gold nanoparticles. J. Am. Chem. Soc. **130**(25), 8038–8043 (2008)
23. Z. Li et al., From redox gating to quantized charging. J. Am. Chem. Soc. **132**(23), 8187–8193 (2010)
24. H.L. Jiang et al., Synergistic catalysis of Au@Ag core-shell nanoparticles stabilized on metal-organic framework. J. Am. Chem. Soc. **133**(5), 1304–1306 (2011)
25. R.W.J. Scott et al., Bimetallic palladium—Gold dendrimer-encapsulated catalysts. J. Am. Chem. Soc. **126**(47), 15583–15591 (2004)
26. T. Shibata et al., Size-dependent spontaneous alloying of Au-Ag nanoparticles. J. Am. Chem. Soc. **124**(40), 11989–11996 (2002)
27. J. Gao et al., Colloidal stability of gold nanoparticles modified with thiol compounds: bioconjugation and application in cancer cell imaging. Langmuir **28**(9), 4464–4471 (2012)
28. J. Bao et al., Bifunctional Au-$Fe_3O_4$ nanoparticles for protein separation. ACS Nano **1**(4), 293–298 (2007)
29. C.S. Levin et al., Magnetic–plasmonic core–shell nanoparticles. ACS nano **3**(6), 1379–1388 (2009)
30. T.A. Larson et al., Hybrid plasmonic magnetic nanoparticles as molecular specific agents for MRI/optical imaging and photothermal therapy of cancer cells. Nanotechnology **18**(32), 325101 (2007)
31. P.K. Jain et al., Surface plasmon resonance enhanced magneto-optics (SuPREMO): Faraday rotation enhancement in gold-coated iron oxide nanocrystals. Nano Lett. **9**(4), 1644–1650 (2009)
32. F. Pineider et al., Spin-polarization transfer in colloidal magnetic-plasmonic au/iron oxide hetero-nanocrystals. ACS Nano **7**(1), 857–866 (2013)
33. I. Mahapatra et al., Probabilistic modelling of prospective environmental concentrations of gold nanoparticles from medical applications as a basis for risk assessment. J. Nanobiotechnol. **13**(1), (2015)
34. V. Amendola et al., Magneto-plasmonic Au-Fe alloy nanoparticles designed for multimodal SERS-MRI-CT imaging. Small **10**(12), 2476–2486 (2014)
35. H. Gao et al., Plasmon-enhanced photocatalytic activity of iron oxide on gold nanopillars. ACS Nano **6**(1), 234–240 (2011)
36. Z. Ban et al., The synthesis of core-shell iron@gold nanoparticles and their characterization. J. Mater. Chem. **15**(43), 4660–4662 (2005)
37. B. Ravel, E. Carpenter, V. Harris, Oxidation of iron in iron/gold core/shell nanoparticles. J. Appl. Phys. **91**(10), 8195–8197 (2002)
38. E.V. Shevchenko et al., Gold/iron oxide core/hollow-shell nanoparticles. Adv. Mater. **20**(22), 4323–4329 (2008)
39. C.L. Ren et al., Facile method for preparing gold coated iron oxide nanoparticles. Mater. Res. Innov. **15**(3), 208–211 (2011)
40. Z. Li, A. Friedrich, A. Taubert, Gold microcrystal synthesis via reduction of HAuCl4 by cellulose in the ionic liquid 1-butyl-3-methyl imidazolium chloride. J. Mater. Chem. **18**(9), 1008–1014 (2008)
41. D. Shore et al., Electrodeposited Fe and Fe–Au nanowires as MRI contrast agents. Chem. Commun. 52, 12634–12637 (2016)
42. S. Scaramuzza, S. Agnoli, V. Amendola, Metastable alloy nanoparticles, metal-oxide nanocrescents and nanoshells generated by

laser ablation in liquid solution: influence of the chemical environment on structure and composition. Phys. Chem. Chem. Phys. **17**(42), 28076–28087 (2015)
43. P. Mukherjee et al., Formation of non-equilibrium Fe-Au solid solutions in nanoclusters. Appl. Phys. Lett. **102**(24), 243103 (2013)
44. F. Mafuné et al., Formation of gold nanoparticles by laser ablation in aqueous solution of surfactant. J. Phys. Chem. B **105**(22), 5114–5120 (2001)
45. T. Sakka et al., Laser ablation at solid-liquid interfaces: an approach from optical emission spectra. J. Chem. Phys. **112**(19), 8645–8653 (2000)
46. S. Barcikowski, G. Compagnini, Advanced nanoparticle generation and excitation by lasers in liquids. Phys. Chem. Chem. Phys. **15**(9), 3022–3026 (2013)
47. G. Compagnini, A.A. Scalisi, O. Puglisi, Ablation of noble metals in liquids: A method to obtain nanoparticles in a thin polymeric film. Phys. Chem. Chem. Phys. **4**(12), 2787–2791 (2002)
48. S. Reich et al., Pulsed laser ablation in liquids: Impact of the bubble dynamics on particle formation. J. Colloid Interface Sci. **489**, 106–113 (2017)
49. J. Zhang, C.Q. Lan, Nickel and cobalt nanoparticles produced by laser ablation of solids in organic solution. Mater. Lett. **62**(10–11), 1521–1524 (2008)
50. J. Zhang, M. Chaker, D. Ma, Pulsed laser ablation based synthesis of colloidal metal nanoparticles for catalytic applications. J. Colloid Interface Sci. **489**, 138–149 (2017)
51. V. Amendola, M. Meneghetti, Laser ablation synthesis in solution and size manipulation of noble metal nanoparticles. Phys. Chem. Chem. Phys. **11**(20), 3805–3821 (2009)
52. G. Palazzo et al., On the stability of gold nanoparticles synthesized by laser ablation in liquids. J. Colloid Interface Sci. **489**, 47–56 (2017)
53. V. Amendola et al., Formation of alloy nanoparticles by laser ablation of Au/Fe multilayer films in liquid environment. J. Colloid Interface Sci. **489**, 18–27 (2017)
54. Z. Sheykhifard et al., Direct fabrication of Au/Pd(II) colloidal core-shell nanoparticles by pulsed laser ablation of gold in PdCl2 Solution. J. Phys. Chem. C **119**(17), 9534–9542 (2015)
55. J. Liao et al., Linear aggregation of gold nanoparticles in ethanol. Colloids Surf., A **223**(1–3), 177–183 (2003)
56. K.G. Moodley, M.J. Nicol, Kinetics of reduction of gold (III) by platinum (II) and iron (III) in aqueous chloride solutions. J. Chem. Soc., Dalton Trans. 10, 993–996 (1977)
57. A. Letzel et al., Size quenching during laser synthesis of colloids happens already in the vapor phase of the cavitation bubble. J. Phys. Chem. C **121**(9), 5356–5365 (2017)
58. S. Petersen, S. Barcikowski, In situ bioconjugation: single step approach to tailored nanoparticle-bioconjugates by ultrashort pulsed laser ablation. Adv. Funct. Mater. **19**(8), 1167–1172 (2009)